

**Top quark anomalous couplings at the International Linear Collider**

Erik Devetak and Andrei Nomerotski

*Oxford University, Denys Wilkinson Building, Keble Road, Oxford OX1 3RH, United Kingdom*

Michael Peskin

*SLAC, Stanford University, 2575 Sand Hill Road, Menlo Park, California 94025, USA*

(Received 12 May 2010; published 17 August 2011)

We present a study of the experimental determination of the forward-backward asymmetry in the process  $e^+e^- \rightarrow t\bar{t}$  and in the subsequent  $t \rightarrow Wb$  decay, studied in the context of the International Linear Collider. This process probes the elementary couplings of the top quark to the photon, and the  $Z$  and the  $W$  bosons at a level of precision that is difficult to achieve at hadron colliders. Measurement of the forward-backward asymmetry requires excellent  $b$  quark identification and determination of the quark charge. The study reported here is performed in the most challenging all-hadronic channel  $e^+e^- \rightarrow b\bar{b}q\bar{q}q\bar{q}$ . It includes realistic details of the experimental environment, a full Monte Carlo simulation of the detector, based on the Silicon Detector concept, and realistic event reconstruction. The forward-backward asymmetries are determined to a precision of approximately 1% for each of the two choices of beam polarization. We analyze the implications for the determination of the  $t\bar{t}Z$  and  $Wt\bar{b}$  couplings.

DOI: [10.1103/PhysRevD.84.034029](https://doi.org/10.1103/PhysRevD.84.034029)

PACS numbers: 14.65.Ha

**I. INTRODUCTION**

The top quark is substantially more massive than the other known quarks. Simply by virtue of this fact, the top quark couples more strongly to the particles that generate the spontaneous symmetry breaking of the electroweak interactions. It is possible that the large mass of the top quark is explained by new interactions of the top quark. It is thus important to measure the properties of the top quark carefully, searching for signals of special interactions of this quark.

Particularly interesting quantities to study are the form factors that describe the coupling of the top quark to elementary currents. These are the analogues for any new interactions of the proton form factors, which played such a large role in the elucidation of QCD. We will study the process  $e^+e^- \rightarrow t\bar{t}$ . In this reaction, two sets of form factors enter, the form factors that describe the  $\gamma$  and  $Z$  couplings to  $t\bar{t}$ , which describe the  $t\bar{t}$  production vertex, and the form factors that describe the  $W$  coupling to  $t\bar{b}$ , which describe the  $t$  and  $\bar{t}$  decay vertices. As a matter of principle, a full reconstruction of the  $t\bar{t}$  system in  $e^+e^-$  annihilation can give information on both sets of vertices. The effects of the possible form factors on observables of the  $t\bar{t}$  system have been studied by many authors, for example, [1–7]. Some of these couplings will be constrained at the LHC, but others are very difficult to access there. In particular, the vector and axial vector couplings of the top quark to the  $Z$  boson are shifted by new physics effects in many models [8–10]. However, these couplings are very difficult to measure precisely at the LHC, and the associated form factors are completely inaccessible at values of  $Q^2$  larger than  $m_Z^2$ .

In this paper, we will begin a study of the determination of these form factors under realistic experimental conditions at the proposed future  $e^+e^-$  collider, the International Linear Collider (ILC). We will make use of the detector model given by the Silicon Detector (SiD) concept and the set of full-simulation tools developed for the benchmarking of SiD [11]. These tools provide a very detailed simulation of the experimental environment at the ILC.

We will consider the forward-backward asymmetries both for the  $b$  and  $\bar{b}$  quarks and for the  $t$  and  $\bar{t}$  quarks. In each case, the forward-backward asymmetry is defined as

$$A_{fb} = \frac{\sigma(\theta < 90^\circ) - \sigma(\theta > 90^\circ)}{\sigma(\theta < 90^\circ) + \sigma(\theta > 90^\circ)}, \quad (1)$$

where  $\sigma(\theta < 90^\circ)$  is the cross section of the events in which the  $b$  or  $t$  quark has a polar angle of less than  $90^\circ$  in the center of mass frame of reference. The standard spherical coordinate system convention is used to define  $\theta$ . This asymmetry measurement is a complex analysis in a dense multijet environment. Typical events have six-jet final states. Flavor tagging must be done to identify the  $b$  quark jets and resolve the combinatoric ambiguities. Quark charges must be measured to distinguish the  $t$  and  $\bar{t}$  decay products. Detector resolution and acceptance, together with nonideal efficiency and purity of the reconstruction algorithms, could play a critical role in determining the ultimate sensitivity of the measurement and hence its physics reach. This study addresses these issues for the first time. Our conclusion is that, with the beam conditions and integrated luminosities that the ILC will provide, a well-designed detector can overcome these potential

problems and realize the small measurement uncertainties that were projected in parametric studies.

The paper is organized as follows: Sec. II gives general parameters of top quark production at the ILC. Section III introduces the SiD detector concept. Section IV presents the software framework used in this analysis. Section V describes the signal selection and the calculation of the cross section for the fully hadronic  $t\bar{t}$  final state. This section also discusses the flavor-tagging method and its performance. Section VI is devoted to the quark charge reconstruction algorithms, which are fundamental to the analysis. The results for forward-backward asymmetries are presented in Sec. VII. Section VIII puts these results into context by interpreting them as bounds on deviations of the  $Zt\bar{t}$  and  $Wtb$  form factors from their standard model values. Section IX gives our conclusions.

## II. TOP QUARK AT THE ILC

The International Linear Collider is a proposed electron-positron accelerator operating in the center of mass energy range  $\sqrt{s} = 200 \text{ GeV} - 500 \text{ GeV}$ . An upgrade to the center of mass energy of 1 TeV is also envisaged, as are possible calibration runs at the Z boson mass energy [12]. The maximum design luminosity is  $2 \times 10^{34} \text{ cm}^{-2} \text{ s}^{-1}$ . In the analysis presented here the center of mass energy and total integrated luminosity were assumed to be, respectively, 500 GeV and  $500 \text{ fb}^{-1}$ , the latter one equivalent to a few years of ILC running.

The top quark at the ILC, assuming the 500 GeV operation, is mainly produced in pairs through the  $e^+e^- \rightarrow Z \rightarrow t\bar{t}$  and  $e^+e^- \rightarrow \gamma \rightarrow t\bar{t}$  processes. The theoretical total cross section of top quark pair production is approximately  $600 \text{ fb}$  [13]. Although this value is substantially lower than the one at the LHC, the clean environment, well-defined initial state, and polarization make the ILC an ideal machine to perform top quark precision measurements.

## III. THE SID DETECTOR CONCEPT

The top quark properties are studied with the concept of the Silicon Detector, which is a general purpose detector designed to perform precision measurements and, at the same time, be sensitive to a wide range of possible new phenomena [11]. It is based on a five layer silicon pixel vertex detector, silicon tracking with single bunch time stamping capabilities, silicon-tungsten electromagnetic calorimetry, and a highly segmented hadronic calorimeter. The particle flow algorithm (PFA) [14] is an important strategy driving the basic philosophy and layout of the detector. SiD also incorporates a five Tesla solenoid, an iron flux return, and a muon identification system. A schematic view of the SiD quadrant is shown in Fig. 1.



FIG. 1 (color online). Disposition of subdetectors in the SiD quadrant. All dimensions are in mm.

## IV. ANALYSIS FRAMEWORK

The event generation has been performed using the WHIZARD Monte Carlo (MC) generator [15,16]. Event samples were created with the expected ILC baseline parameters of 80% electron and 30% positron polarization. Half of the event sample was created with a positive electron and negative positron polarization, while the other half has been created with a negative electron and positive positron polarization.

WHIZARD was used to generate samples of all zero, two, four, and six fermion final states as well as top quark-dominated eight fermion processes. This generation used electroweak vertices only, with gluon emission turned off. The intent of this strategy was to correctly describe multifermion processes such as return to the Z ( $e^+e^- \rightarrow \gamma^* Z^* \rightarrow 4$  fermions) and similar processes with intermediate off-shell W bosons. These reactions with t-channel exchange and off-shell electroweak bosons are the most important backgrounds to multifermion  $e^+e^-$  annihilation processes. QCD was included in the events by using PYTHIA to evolve final-state quarks through parton showering, fragmentation, and decay. PYTHIA [17] was also used to generate final-state photon radiation. There is no double-counting of multifermion production between the WHIZARD stage and the parton shower stage. This procedure treats multigluon radiation only approximately and ignores quantum interference between the electroweak and QCD production amplitudes. However, these are relatively small effects at the ILC and are unimportant except in dedicated QCD studies.

About  $7 \times 10^6$  events were created and processed through the full GEANT 4 [18] detector simulation, with individual events weighted to reflect the statistical sampling. However all of the six and eight fermion states, the ones most relevant for the analysis, were left unweighted.

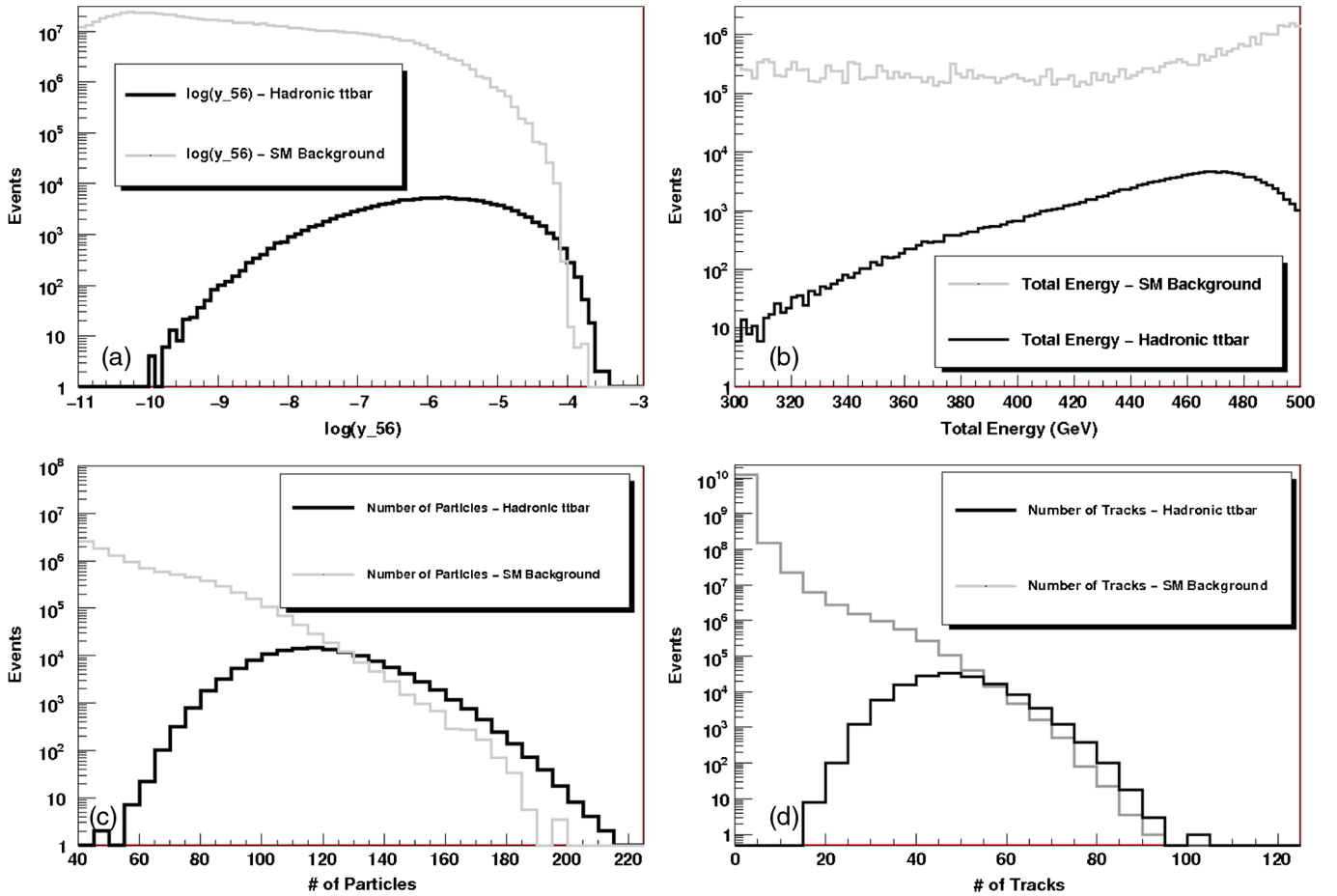


FIG. 2 (color online). Kinematic and topological event selections: (a)  $y_{56}$ , (b) total energy, (c) number of particles in the event, and (d) number of tracks in the event.

The sample has been subsequently divided into  $b\bar{b}q\bar{q}q\bar{q}$  final states, which constitute the signal and all remaining events representing the background.

In addition to these “pseudo data” events a further independent sample of  $2 \times 10^6$   $b\bar{b}f\bar{f}f\bar{f}$  events was used for the calibration of algorithms.

The jet clustering algorithm used in this analysis is the  $y$ -cut algorithm [19] with the number of jets fixed at six to match the number of jets expected for a hadronic  $t\bar{t}$  event.

## V. TOP QUARK SELECTION AND $e^+e^- \rightarrow t\bar{t} \rightarrow b\bar{b}q\bar{q}q\bar{q}$ CROSS SECTION

The analysis starts with a simple event selection based on several global variables described below. Events with isolated leptons, defined as a jet containing only one reconstructed particle which is either an electron or a muon, are rejected, as only the  $b\bar{b}q\bar{q}q\bar{q}$  final state was considered.

Subsequently, a set of kinematic and topological discriminating variables has been defined: the total energy of the event; the jet finder  $y_{56}$  parameter, which represents the  $y$ -cut separation between the five and six jet hypothesis; the

number of particles; and the number of tracks. The number of particles in the event is defined as the number of reconstructed particles identified by the PFA. Figure 2 shows distributions of these variables for the signal and background samples before any selections.

Table I presents the kinematic and topological event selections that have been used. After this stage all but 492 000 background events have been rejected. This compares to the initial number of  $12.5 \times 10^9$  events. The efficiency loss for the initial 143 000 signal events due to this procedure is equal to 9.7%. The subsequent stage of the analysis aims to identify the  $b$  quarks and to identify the  $W$  bosons exploiting its significant invariant mass.

TABLE I. List of the kinematic and topological event selections.

$E_{\text{tot}}$	>	400 GeV
$\log(y_{56})$	>	-8.5
Number of particles in event	>	80
Number of tracks in event	>	30

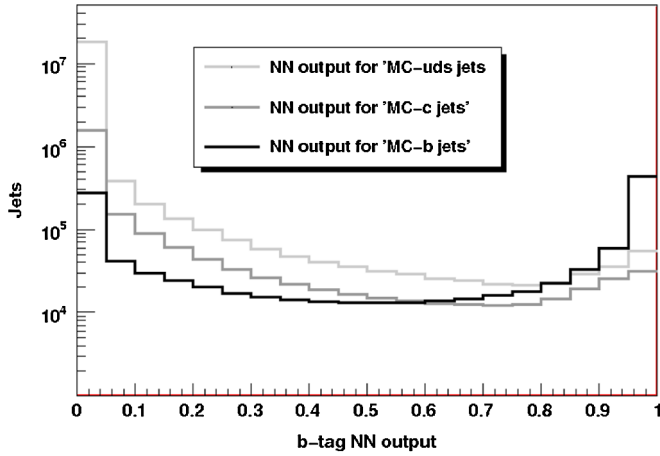


FIG. 3 (color online). Distribution of the flavor-tagging neural network output for  $uds$ ,  $c$ , and  $b$  quark jets.

For the purpose of  $b$  quark identification the output of the Linear Collider Flavour Identification (LCFI) flavor-tagging algorithm [20] has been used with the default settings. Figure 3 shows the performance of the LCFI  $b$ -tagging algorithm when used for a  $e^+e^- \rightarrow t\bar{t} \rightarrow b\bar{b}q\bar{q}q\bar{q}$  sample. The neural network output for  $uds$ ,  $c$  and  $b$  quark jets demonstrates a good separation of different quark flavors for a multijet environment. In numerical terms, a selection corresponding to the  $b$  quark-tagging efficiency of 45.0% will tag 2.6% of charm quarks and 0.8% of light quarks [21].

Three additional event selections have been applied to the remaining events. The sum of the  $b$ -tag neural network outputs of all six jets has been required to be higher than 1.5; the  $b$ -tag parameter of the most  $b$ -like and second most  $b$ -like jet has been required to be at least 0.9 and 0.4, respectively. Figure 4 shows the sum of the  $b$  tag of the neural network outputs of all six jets for the signal and background events after the kinematic and topological event

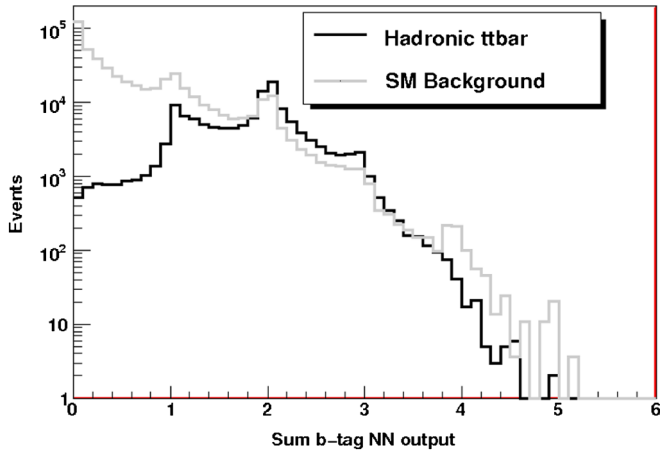


FIG. 4 (color online). The sum of the  $b$ -tag neural network outputs of all six jets for the signal and the background events after the kinematic and topological event selection.

selection and before any  $b$ -tagging selection. It is clear that this is a powerful discriminant to select a clean  $t\bar{t}$  sample. In order to identify the invariant mass of the reconstructed  $W$  bosons, the KinFit kinematic fitting algorithm [22] has been used with a single constraint that the masses of the two  $W$  bosons are equal. Only the four least  $b$ -like jets have been considered for the fit in order to reduce the number of combinations. All the events with a  $W$  mass of more than 110 GeV or less than 50 GeV have been rejected.

After the  $b$  quark and  $W$  boson identification procedure, approximately 74 000  $b\bar{b}q\bar{q}q\bar{q}$  signal and 33 500 background events have passed all selections corresponding to a signal efficiency of 51.5% and purity of 68.8%. A significant proportion of the remaining background derives from the  $W^+W^- \rightarrow q\bar{q}q\bar{q}$  and  $b\bar{b}l\nu q\bar{q}$  events, with a smaller contribution from  $ZZ \rightarrow q\bar{q}q\bar{q}$ .

The top quark mass has been reconstructed using the same kinematic fitting approach. The primary aim of this procedure was to find a correct match of the  $b$  quarks to the corresponding  $W$  boson, which will be required when the polar angle of the top quark needs to be reconstructed later in the analysis. The reconstructed top mass was also used to further suppress the background rejecting all events with masses lower than 145 GeV and higher than 195 GeV. Events that yield a probability of less than 1% with respect to the constraints used for the fitting are also rejected. All constraints used for the top mass kinematic fitting can be found in Table II. The final efficiency of the whole selection process is 29.8% for a purity of 79.7%.

Once the event selection has been performed it is relatively straightforward to calculate the cross section of the  $e^+e^- \rightarrow t\bar{t} \rightarrow b\bar{b}q\bar{q}q\bar{q}$  process by the simple use of the following formula:

$$\sigma = \frac{N_{\text{ALL}} - N_{\text{BG}}}{\epsilon \int L dt}, \quad (2)$$

where  $N_{\text{ALL}}$  is the total number of observed events, while  $N_{\text{BG}}$  is the number of simulated background events,  $\epsilon$  is the signal selection efficiency, and  $\int L dt$  is the integrated luminosity. Under the assumption that the signal efficiency and the integrated luminosity can be determined with negligible errors and that the background can be reliably determined and subtracted, the statistical error on the cross section is equal to  $\sqrt{N_{\text{ALL}}}/(\epsilon \int L dt)$ . The cross section has

TABLE II. List of kinematic fitting constraints used for the calculation of the top mass.

Mass (top 1)	=	Mass (top 2)
Mass (W1)	=	80.4 GeV
Mass (W2)	=	80.4 GeV
Mass ( $b_{\text{Jet 1}}$ )	=	5.8 GeV
Mass ( $b_{\text{Jet 2}}$ )	=	5.8 GeV
$E_{\text{Total}}$	=	500 GeV
$p_x; p_y; p_z$	=	0



been calculated to be  $287.4 \pm 1.3$  fb for the whole sample, and  $370.5 \pm 1.6$  fb and  $204.3 \pm 1.2$  fb for the two different polarization samples, the first cross section being for the sample with negative electron polarization. It has to be noticed that these are the cross sections for the  $e^+e^- \rightarrow t\bar{t} \rightarrow b\bar{b}q\bar{q}q\bar{q}$  process and not for  $t\bar{t}$  production.

## VI. QUARK CHARGE RECONSTRUCTION

The next step in the analysis is the reconstruction of the quark charge which is necessary to determine the forward-backward asymmetry of the bottom and top quarks. Hadronization and fragmentation processes obscure the quark charge since the bottom quarks fragment into neutral mesons in more than 50% of the cases. While charged  $B$  mesons, when reconstructed correctly, allow for unambiguous interpretation of the quark charge, for the neutral  $B$  hadrons the charge is not representative of the quark charge. Moreover, the neutral  $B$  mesons oscillate, which further dilutes the charge reconstruction.

Several variables sensitive to the charge have been studied, and an efficient quark charge estimator has been devised as a combination of two variables, the vertex charge and jet charge, as described below. Note that this technique considerably improves a simple vertex charge algorithm used in the LCFI Vertex software [20].

### A. Vertex charge and jet charge algorithms

The vertex charge algorithm uses all tracks associated with a secondary vertex weighted by their momentum to define the vertex charge  $Q_{\text{VTX}}$  as per the following formula:

$$Q_{\text{VTX}} = \frac{\sum_j p_j^k Q_j}{\sum_j p_j^k}, \quad (3)$$

where  $Q_j$  is the charge of the  $j$ th track,  $p_j$  is the momentum of the track, and  $k$  is a user defined parameter; the sums are performed only on the tracks associated with the vertex. The  $k$  parameter was chosen at 0.3 after optimization. The performance of such a method for discriminating the parton charge in the signal sample can be seen in Fig. 5(a). Only genuine, identified at the MC level  $b$  quark jets, with a neural net  $b$  tag higher than 0.4 were included; no further requirements have been imposed to the  $b$  quark final state.

Another method of the quark charge determination implemented in the analysis, the momentum weighted jet charge [23], is similar to the one already described in Eq. (3), with the only difference in the track selection process which now includes all the tracks present in a jet rather than in a vertex. The jet charge algorithm recovers 3.2% of identified  $b$  jets which do not have a secondary vertex.

The performance of the algorithm can be seen in Fig. 5(b). Also in this case, the optimal value for the  $k$  parameter has been determined to be 0.3.

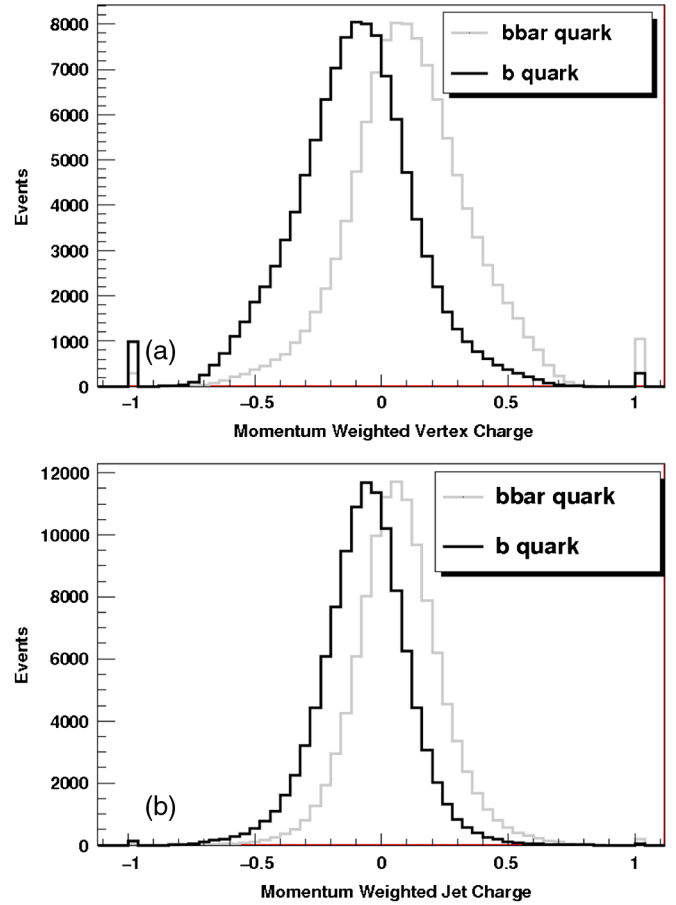


FIG. 5 (color online). Distributions of reconstructed charge for the template signal sample for  $b$  quark and  $\bar{b}$  quark jets (a) using the momentum weighted vertex charge and (b) using the momentum weighted jet charge.

The two algorithms rely on different principles to identify the quark charge. The jet charge algorithm exploits the kinematic consideration that the most energetic hadrons have a higher probability of containing the charge of the quark that initiated the jet [24]. The principle behind the vertex charge algorithm is instead based on precisely determining all the tracks that derive from the displaced vertex due to the  $b$  quark considerable lifetime. In this case the aim is to directly determine the charge of the meson while the momentum weighting folds in information on the reliability of the track.

It is expected that the vertex charge algorithm is sensitive only to the charged  $B$  mesons, while the jet charge algorithm is more universal for different  $B$ -hadron species. The performance of the algorithms has therefore been tested for only charged mesons  $B^+$  and  $B^-$  and for only neutral mesons  $B^0$  and  $\bar{B}^0$ . Figure 6(a) shows the purity of a sample with a certain quark charge as a function of selection efficiency. This demonstrates that the momentum weighted vertex charge is able to distinguish well between  $B^+$  and  $B^-$ , while having almost no discriminatory power when it comes to  $B^0$  and  $\bar{B}^0$ .

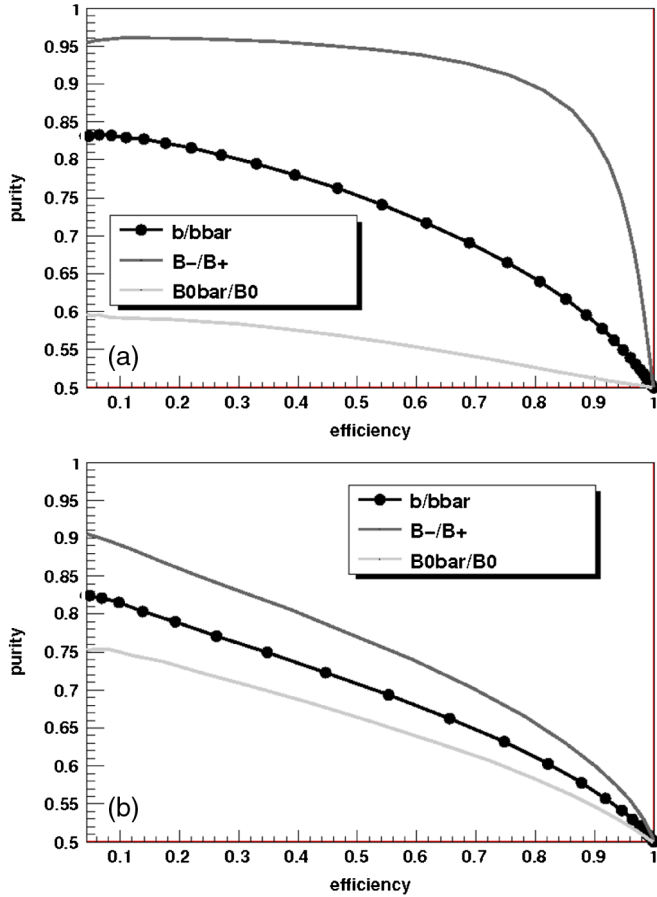


FIG. 6 (color online). Performance of (a) momentum weighted vertex charge and (b) momentum weighted jet charge in distinguishing  $B^+$  from  $B^-$ ,  $B^0$  from  $B^0$ , and  $b$  from  $\bar{b}$ .

Differently, the performance of the momentum weighted jet charge, Fig. 6(b), is more similar between the two cases, and the algorithm can separate reasonably well also  $B^0$  and  $\bar{B}^0$ , which include both  $B_d^0$  and  $B_s^0$  mesons. Most of the difference between the charged and neutral mesons in this case can be attributed to the flavor oscillations of neutral mesons. While in this process the charge of the meson does not change, the charge of the  $b$  quark does. This introduces a further dilution in the charge discrimination. The effect is rather small in the  $B_d^0$  mesons, which have a period of oscillation larger than their mean lifetime. In the case of  $B_s^0$  mesons the effect is dominant, as oscillations are much faster than the meson lifetime.

### B. Combined charge

As the two different methods rely on different information and are rather independent, they have been combined into a single discriminant, based on the probability ratios [25]. If  $f_i^b(x_i)$  is the probability density function for the  $b$  quark for variable  $x_i$  and  $f_i^{\bar{b}}(x_i)$  is the equivalent distribution for the  $\bar{b}$  quark, then for each discriminating variable  $x_i$ , their ratio  $r_i$  is defined as

$$r_i(x_i) = \frac{f_i^{\bar{b}}(x_i)}{f_i^b(x_i)}, \quad (4)$$

where the index  $i$  denotes the discriminating variable. Distributions of  $f^b$  and  $f^{\bar{b}}$  were determined using independent samples.

For each data event a combined tagging variable can then be defined:

$$r = \prod_i r_i. \quad (5)$$

The range of possible values for  $r$  is between 0 and  $\infty$ . Given the definition of  $r$ , if  $r < 1$  then the reconstructed jet is more likely to be from a  $b$  quark, and if  $r > 1$  the jet is more likely to originate from a  $\bar{b}$  quark. For convenience, a variable  $C$  changing between  $-1$  and  $+1$  has been defined as

$$C = \frac{1 - r}{1 + r}. \quad (6)$$

A jet with  $C > 0$  is more likely to derive from a  $b$  quark, and a jet with  $C < 0$  is more likely to derive from a  $\bar{b}$  quark.

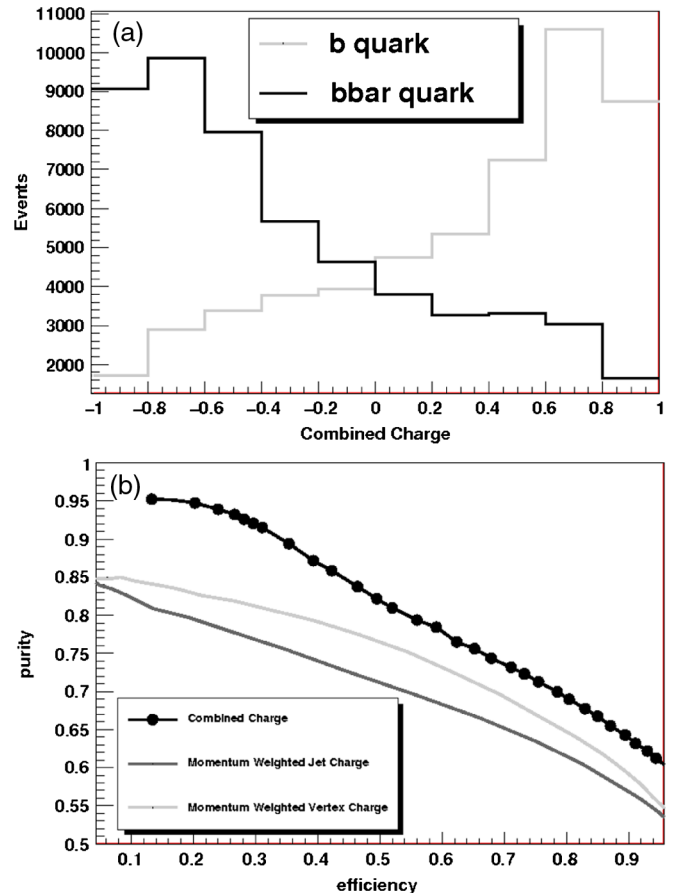


FIG. 7 (color online). Combined charge (a) distributions for  $b$  quark and  $\bar{b}$  quark jets, and (b) purity versus efficiency curves for  $b$  quark and  $\bar{b}$  quark jets for combined charge, momentum weighted vertex charge, and momentum weighted jet charge, shown for the 174.0 GeV sample after all event selections have been applied.

Figure 7(a) shows the combined quark charge performance for the 174.0 GeV top quark sample after all event selections have been applied. Figure 7(b) instead shows the purity versus efficiency curves for the combined charge algorithm in the same sample when compared to standalone momentum weighted vertex charge and momentum weighted jet charge algorithms, as can be seen in Fig. 7(b). The algorithm efficiency is improved by 4% to 10% for a purity range from 60% to 80%.

The method described above allows a straightforward inclusion of other quark charge discriminants such as the lepton charge [25] and dipole charge [26].

## VII. QUARK FORWARD-BACKWARD ASYMMETRIES

### A. Bottom quark forward-backward asymmetry

Before calculating the forward-backward asymmetries for the  $b$  and the  $t$  quark, the possibility of performing an event selection based on the reconstructed charge of the quarks has been investigated. For this purpose one would like to use the information derived from both jets. Assuming that the event is actually a  $b\bar{b}q\bar{q}q\bar{q}$ , rather than an event from the SM background, and that the quark identification has been correctly performed, the charge calculations performed on the two  $b$  jets are really two uncorrelated measurements of the same quantity. The two  $b$  jets must, in fact, have opposite absolute values for their charge.

The combined charges of the two jets with the highest neural net  $b$  tags are therefore multiplied and used as an event selection parameter. Figure 8 shows such a distribution for the signal events with explicit contributions from misidentified events where the misidentification occurred either in the  $b$  tagging (mistagged) or in the quark charge determination (wrong charge). The main aim of this procedure would be not to reject the SM background but rather to

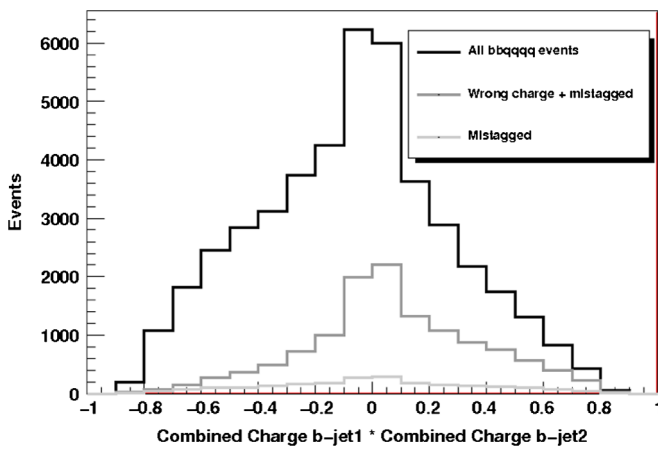


FIG. 8 (color online).  $(\text{Combined charge } b\text{-jet1}) \times (\text{Combined charge } b\text{-jet2})$  distribution for reconstructed events, mistagged events, and events with misidentified charge. Only  $b\bar{b}q\bar{q}q\bar{q}$  signal events are used.

suppress the events in which the  $b$  quark has been mistagged or the charge of such a quark has been misreconstructed. An event charge is labeled as misreconstructed when the reconstructed combined charge of the  $\bar{b}$  quark jet is higher than the combined charge of the  $b$  quark jet.

An optimization has been attempted and the value of  $S/\sqrt{S+B}$  has been maximized, where  $S$  is the number of signal events and  $B$  is the number of background events including both the SM background and mistagged events. Interestingly enough, the optimization suggested that all events should be included. Under these conditions the total signal efficiency is 22.7%, while the signal purity is 58.1%. The impurities derive 45.9% from the SM background, 45.0% from the charge misreconstruction, and 9.1% from the  $b$  quark misidentification.

The calculation of the forward-backward asymmetry as defined in Eq. (1) can now be performed using two jets with the highest values of neural net  $b$  tags. The jet with a higher combined charge has been declared as originating from a  $b$  quark, while the other  $b$  jet has been declared as originating from a  $\bar{b}$  quark. The angle  $\theta$  of the reconstructed  $b$  jet has been used as an approximation of the original  $b$  quark angle. Figure 9 shows the event distribution with respect to  $\cos(\theta)$  of the signal and background events after all selections. The mistagged and SM backgrounds peak in the forward regions where the asymmetry is maximal. This emphasizes the importance of the forward region in the detector design considerations. Note that the mistagged events in the distribution include a contribution from  $\bar{b}$  quarks which peaks at  $\theta = -1$ . This explains a relatively high mistagging rate at  $\theta = -1$  when compared to the number of  $b$  quarks from the signal. It is because of this reason that in the  $\theta = 1$  region the purity exceeds 60%, while in the  $\theta = -1$  region it is only 15%.

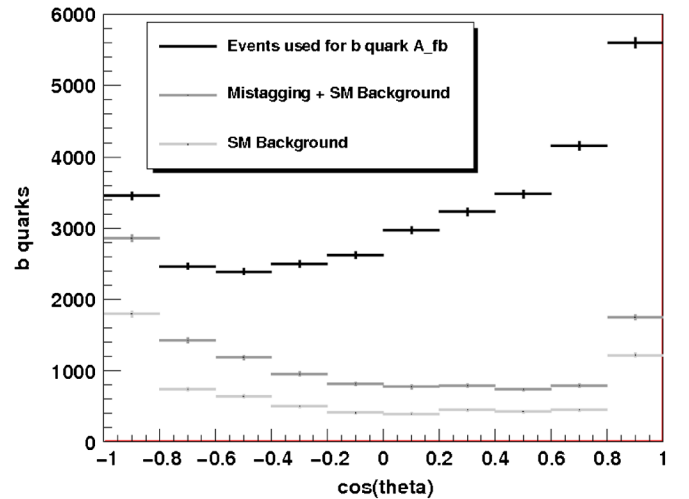


FIG. 9 (color online). Number of events used for the calculation of the  $b$  quark  $A_{fb}$  as a function of the  $b$  quark  $\theta$  angle. In order to qualify as a  $b$  rather than  $\bar{b}$  quark, the combined charge of the jet must be higher than the one of the other  $b$  jet present in the event. The mistagging refers to both quark charge and flavor.

The  $A_{fb}$  calculation proceeds as follows. The number of correctly reconstructed  $b\bar{b}q\bar{q}q\bar{q}$  events is evaluated for the forward and backward hemispheres independently. For this the SM background is subtracted from the total number of reconstructed events. The number of events left is then multiplied by the purity of the reconstruction, accounting for all the events where the charge has been misidentified or where the  $b$  jet has been mistagged. The number of correctly identified  $b$  jets is  $N_b = (N_{\text{tot}} - N_{\text{SM}}) * p$ , where  $N_{\text{tot}}$  is the total number of reconstructed events,  $N_{\text{SM}}$  is the SM background, and  $p$  is the purity of the reconstruction. This equation is applied to each hemisphere, and correspondingly, separate purities have been calculated for the forward and the backward hemispheres. In principle, the number of events should also be corrected for the signal efficiency because Eq. (1) uses the cross sections. However, the efficiencies in the forward and backward regions, to a good approximation, cancel each other out and produce a negligible effect on the final result. This also leads to robustness of the measurement to variations of fragmentation and hadronization models, which results in a negligible systematic uncertainty. Table III shows the  $A_{fb}$  results for different event selections. The first row corresponds to the case of no selection, which maximizes the sensitivity as discussed above [27–30].

For each event selection the uncertainty has been calculated with three different assumptions. The lowest uncertainty,  $\sigma_1$ , assumes that the efficiency of tagging and the standard model background have been perfectly simulated at the MC level and therefore do not contribute to the uncertainty of the forward-backward asymmetry. The only uncertainty contribution therefore is  $\sqrt{N_{\text{tot},\theta < (>)90^\circ}}$ , where  $N_{\text{tot},\theta < (>)90^\circ}$  is the total number of events with  $b$  quarks reconstructed in the forward (backward) region of the detector. For the second evaluation,  $\sigma_2$ , the statistical uncertainty from the  $b$ -tagging efficiency is added in quadrature to the value of  $\sigma_1$ . The added statistical uncertainty is calculated from the previously mentioned *ad hoc* generated calibration sample. Finally, the third evaluation,  $\sigma_3$ , also considers an additional contribution from the statistics of background samples [21], which is added in quadrature to  $\sigma_2$ . In each of the three cases the uncertainty has been calculated separately for the forward and backward regions, and subsequently, the standard error propagation has been used to evaluate the  $A_{fb}$  uncertainty.

TABLE III. Reconstructed  $A_{fb}$  for the  $b$  quark and the respective uncertainties. The different uncertainties ( $\sigma_1, \sigma_2, \sigma_3$ ) have been calculated with different assumptions as explained in the text.

Event selection	$A_{fb}$	$\sigma_1$	$\sigma_2$	$\sigma_3$
Charge $b_1 \times$ Charge $b_2 < 1.0$	0.293	0.006	0.007	0.008
Charge $b_1 \times$ Charge $b_2 < 0.5$	0.293	0.006	0.007	0.008
Charge $b_1 \times$ Charge $b_2 < 0.0$	0.289	0.007	0.008	0.009

The calculated asymmetry agrees well with the initial asymmetry at the MC level, 0.291, which suggests that the performed analysis has not introduced any systematic bias. In order to check for any significant detector smearing leading to systematic effects in  $A_{fb}$ , the angular resolution of the  $b$  jet  $\theta$  angle with respect to the original  $b$  quark has been determined. The resolution has been found to be 0.08 rad, and therefore its effect on the reconstructed asymmetry is negligible.

Finally, the result can also be decomposed with respect to the different polarizations used. In the case of  $-80\%$  electron polarization and  $+30\%$  positron polarization, the asymmetry has been calculated to be 0.356 with an uncertainty of 0.010. In the case  $+80\%$  electron polarization and  $-30\%$  positron polarization, the asymmetry has been calculated to be 0.155 with an uncertainty of 0.012. In both cases the  $\sigma_3$  definition of error is being used.

## B. Top quark forward-backward asymmetry

The analysis of the top quark asymmetry is similar to the one already presented for the  $b$  quark. The only added complication is that, differently from the  $b$  quark, where the angle  $\theta$  of the  $b$  jet can be used as a very good approximation to the angle  $\theta$  of the original  $b$  quark, the direction of the top quark must be reconstructed from its decay products, using the kinematic fitter to determine correct pairing of two  $b$  quarks and two  $W$  bosons. More specifically, the direction of the top quark is calculated from the combination of jets that minimizes the  $\chi^2$  of the fit given the constraints stated in Table II.

The charge of the top quark is determined through the charge of the daughter  $b$  quark. If a reconstructed  $b$  quark jet is part of the three jets used to reconstruct the top quark,

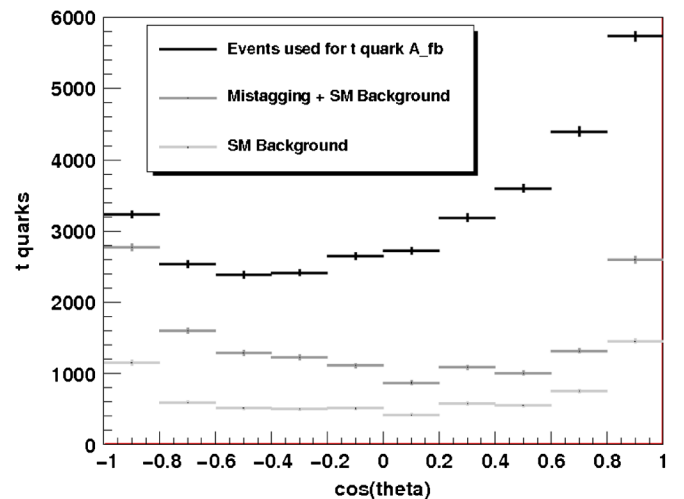


FIG. 10 (color online). Number of events used for the calculation of the top quark  $A_{fb}$  as a function of the top quark  $\theta$  angle. In order to qualify as a  $t$  rather than  $\bar{t}$  quark, the combined charge of the  $b$  jet used to reconstruct the top quark must be higher than the charge of the other  $b$  jet present in the event.



TABLE IV. Reconstructed  $A_{fb}$  for the  $t$  quark and the respective uncertainties. The different uncertainties ( $\sigma_1, \sigma_2, \sigma_3$ ) have been calculated with different assumptions as explained in the text.

Event selection	$A_{fb}$	$\sigma_1$	$\sigma_2$	$\sigma_3$
Charge $b_1 \times$ Charge $b_2 < 1.0$	0.356	0.006	0.007	0.008
Charge $b_1 \times$ Charge $b_2 < 0.5$	0.348	0.006	0.007	0.008
Charge $b_1 \times$ Charge $b_2 < 0.0$	0.353	0.007	0.008	0.009

then the top quark is declared as a  $t$ . If instead a  $\bar{b}$  jet is present, the quark is declared as a  $\bar{t}$ . Given the constraints set to the kinematic fitter only one such quark will be present in each jet. Figure 10 shows the distribution of top quark events with respect to their  $\cos(\theta)$ . The distribution includes the SM and mistagging backgrounds.

Subsequently, the same  $A_{fb}$  calculations have been performed as the ones described in the previous section for the  $b$  quark case with results shown in Table IV. The calculated asymmetry agrees well with the initial one at the MC level, 0.351.

Finally, in the same fashion as for the  $b$  quark, the  $\theta$  angle resolution has been found to be equal to 0.19 rad. This will have a negligible contribution to the total calculated  $A_{fb}$  because only the very central events of the Fig. 10 distribution will ever be smeared enough to change the hemisphere when reconstructed. The asymmetry in this region is, however, small and does not affect the total  $A_{fb}$ .

Similarly to the asymmetry of the bottom quark, the achievable statistical precision has been calculated also for the two cases of polarized beams. Unsurprisingly, values identical to the ones presented for the bottom quark (0.010 and 0.012) have been found.

## VIII. DISCUSSION

To put these results into context, we will interpret them in terms of constraints on the couplings of the top quark to the vector bosons,  $t\bar{t}Z$  and  $Wtb$ .

As we have pointed out already in the Introduction, many models of new physics predict large corrections to the left- and right-handed vector  $t\bar{t}Z$  couplings. The measurement of forward-backward asymmetries in  $e^+e^- \rightarrow t\bar{t}$  will allow these couplings to be determined experimentally in a very direct way.

As a starting point for the analysis, we define the  $\gamma$  and  $Z$  vertex form factors of the top quark by

$$\begin{aligned} \mathcal{L}_{t\bar{t}}^Z = & eA_\mu \bar{t} \left[ \gamma^\mu (P_L F_{L\gamma} + P_R F_{R\gamma}) + i \frac{\sigma^{\mu\nu} q_\nu}{2m_t} F_{2\gamma} \right] t \\ & + eZ_\mu \bar{t} \left[ \gamma^\mu (P_L F_{LZ} + P_R F_{RZ}) + i \frac{\sigma^{\mu\nu} q_\nu}{2m_t} F_{2Z} \right] t, \end{aligned} \quad (7)$$

where  $P_L$  and  $P_R$  are the left- and right-handed chiral projection operators,  $q_\nu$  is the four-momentum of the

virtual photon or  $Z^0$ , and  $\sigma^{\mu\nu} = i/2(\gamma^\mu \gamma^\nu - \gamma^\nu \gamma^\mu)$ . The tree-level standard model values of the form factors are

$$\begin{aligned} F_{L\gamma} = F_{R\gamma} &= \frac{2}{3}, & F_{2\gamma} = F_{2Z} &= 0, \\ F_{LZ} &= \frac{(\frac{1}{2} - \frac{2}{3}s_w^2)}{s_w c_w}, & F_{RZ} &= \frac{(-\frac{2}{3}s_w^2)}{s_w c_w}, \end{aligned} \quad (8)$$

where  $s_w$  and  $c_w$  are the sine and cosine of the Weinberg angle. For later reference, the numerical values of the standard model  $Z$  boson form factors, using  $s_w^2 = 0.231$ , are

$$F_{LZ} = 0.821, \quad F_{RZ} = -0.365.$$

In principle, we could also introduce in each line a fourth,  $CP$ -violating, form factor proportional to  $\sigma^{\mu\nu} \gamma^5$ . One might also include contact interactions between the  $e^+e^-$  and  $t\bar{t}$  states [31].

In principle, a complete helicity analysis of the full set of production and decay angles has the power to constrain many of these parameters independently. However, in this paper, we have concentrated on the experimental measurement of the forward-backward asymmetries. Since our main concern here is to illustrate the power of that measurement, we will choose a parametrization with two free parameters that can be determined in terms of the two top quark forward-backward asymmetries corresponding to two cases of beam polarizations.

In the following, then, we will assume that the  $\gamma t\bar{t}$  form factors take their standard model values given in (8), that the magnetic moment  $Z$  form factor  $F_{2Z}$  is zero, and that the decay form factors take their standard model values. We will allow only values of the  $Z t\bar{t}$  form factors  $F_{LZ}$  and  $F_{RZ}$  to be varied, and we will determine these parameters from two measurements of the  $t\bar{t}$  forward-backward asymmetry with different beam conditions. The choice of  $-80\%$  electron polarization and  $+30\%$  positron polarization leads to  $t\bar{t}$  production dominantly from the initial state  $e_L^- e_R^+$ . In the standard model, for this polarization choice, the  $\gamma$  and  $Z$   $s$ -channel amplitudes interfere constructively for the production of  $t_L \bar{t}_R$  and destructively for the production of  $t_R \bar{t}_L$ , leading to a large positive forward-backward asymmetry. The main effect of changing the  $Z$  form factors is to relax the destructive interference in the production of  $t_R \bar{t}_L$ . Thus, the asymmetry in this polarization state is mainly sensitive to  $F_{RZ}$ , which gives the larger effect on the  $t_R \bar{t}_L$  state. Similarly, the choice of  $+80\%$  electron polarization and  $-30\%$  positron polarization leads to  $t\bar{t}$  production dominantly from the initial state  $e_R^- e_L^+$ . In the standard model, for this polarization choice, the  $\gamma$  and  $Z$   $s$ -channel amplitudes interfere constructively for the production of  $t_R \bar{t}_L$  and destructively for the production of  $t_L \bar{t}_R$ . This also leads to a large positive forward-backward asymmetry, but one that is mainly sensitive to  $F_{LZ}$ . Thus, the measurement of the  $t\bar{t}$  forward-backward asymmetry with

these two beam settings sensitively picks out nonstandard contributions to the two separate  $Zt\bar{t}$  vector form factors [32].

For 100% polarized beams, the sensitivity of the  $t\bar{t}$  forward-backward asymmetries to deviations of the  $Z$  form factors from their standard model values can be computed to be

$$\begin{pmatrix} \delta A_{FB}(LR) \\ \delta A_{FB}(RL) \end{pmatrix} \begin{pmatrix} 0.138 & -0.392 \\ 0.461 & -0.106 \end{pmatrix} \begin{pmatrix} \delta F_{LZ} \\ \delta F_{RZ} \end{pmatrix} \quad (9)$$

using  $\sqrt{s} = 500$  GeV and  $\sin^2\theta_w = 0.231$ . The large off-diagonal terms in this matrix show clearly the effect discussed in the previous paragraph. For an electron polarization of  $-80\%$  and a positron polarization of  $+30\%$ , the fraction of events in the two relevant initial polarization states is

$$\begin{aligned} f(e_L^- e_R^+) &= \frac{(1 + P(e^-))(1 + P(e^+))}{4} = 0.585, \\ f(e_R^- e_L^+) &= \frac{(1 - P(e^-))(1 - P(e^+))}{4} = 0.035. \end{aligned} \quad (10)$$

By taking this into account, it is possible to transform the matrix presented in Eq. (9) in order to account for the beam polarizations actually used. Recomputing the numerator and denominator for  $A_{FB}$ , we find that the relation between the form factor deviations becomes

$$\begin{pmatrix} \delta A_{FB}(LR) \\ \delta A_{FB}(RL) \end{pmatrix} \begin{pmatrix} 0.164 & -0.374 \\ 0.367 & -0.238 \end{pmatrix} \begin{pmatrix} \delta F_{LZ} \\ \delta F_{RZ} \end{pmatrix}. \quad (11)$$

Then the standard uncertainties reported in Sec. VII,

$$\sigma(A_{FB}(LR)) = 0.010, \quad \sigma(A_{FB}(RL)) = 0.012, \quad (12)$$

give the uncertainties on  $\delta F_{LZ}$  and  $\delta F_{RZ}$ ,

$$\sigma(\delta F_{LZ}) = 0.051, \quad \sigma(\delta F_{RZ}) = 0.042, \quad (13)$$

with some correlation between the values. Normalizing to the standard model values of these parameters,

$$\sigma(\delta F_{LZ})/F_{LZ} = 0.062, \quad \sigma(\delta F_{RZ})/F_{RZ} = 0.116. \quad (14)$$

These uncertainties are comparable to the values suggested in [32] on the basis of parametric simulations. One can see, for example, by comparing the models discussed in [10], that such measurements would cut deeply into the space of deviations predicted in models of new physics.

The ILC study of the reaction  $e^+e^- \rightarrow t\bar{t}$  will also include events in which either the  $t$  or the  $\bar{t}$  decays leptonically. These events add a data set of approximately equal size to the one considered here in which the  $t/\bar{t}$  charge discrimination is unambiguous. Thus, the full analysis of the ILC data will be even better at determining the  $Zt\bar{t}$  couplings.

In a similar manner the results can also be interpreted with respect to the  $Wtb$  anomalous couplings. As a matter of fact, the decay form factors of the top quark are already

TABLE V.  $A_{fb}$  asymmetry of the  $b$  quark from the top decay for the standard model and anomalous  $Wtb$  vertices, calculated at a center of mass energy of 500 GeV and in the center of mass rest frame.

$B_R$	$B_L$	$A_{fb}$
0.0	0.0	0.279
0.0	-0.2	0.243
0.0	-0.4	0.218
0.0	-0.6	0.197
0.0	-1.0	0.169
-0.6	0.0	0.301
-1.0	0.0	0.315

constrained at the 20% level by the measurement of the  $W$  helicity at hadron colliders [33], and these measurements will be improved at the LHC. Thus, it is likely that, by the time the ILC operates, the decay form factors could be fixed to experimentally determined values. Nevertheless, for completeness, we consider the effects of these anomalous couplings, following the notation in [4].

In this case the appropriate vertex under consideration is

$$\begin{aligned} L_{tb}^W &= -\frac{g}{\sqrt{2}} \left[ W_\mu^- \bar{b} (\gamma_\mu A_L P_L + \gamma_\mu A_R P_R) t \right. \\ &\quad \left. - \frac{1}{2M_W} W_{\mu\nu}^- \bar{b} \sigma^{\mu\nu} (B_L P_R + B_R P_L) t \right], \end{aligned} \quad (15)$$

where  $W_{\mu\nu} = D_\mu W_\nu - D_\nu W_\mu$ ,  $D_\mu = \partial_\mu - ieA_\mu$ .  $A_{L,R}$  and  $B_{L,R}$  are the coupling form factors. In the standard model  $A_L$  is equal to 1, while all the other form factors are equal to zero.

Table V presents predictions of the  $b$  quark asymmetry for different values of the  $Wtb$  anomalous couplings [4].

It can be inferred from Table V that the measurement of the  $b$  quark forward-backward asymmetry is sensitive to the presence of a  $B_L$  anomalous form factor whose absolute value is greater than approximately 0.05. Measurement of other observables, not considered in this paper, that specifically target the top quark decay properties will put much stronger constraints on both  $B_L$  and  $B_R$ .

Note that there is a difference between the asymmetry predicted by the WHIZARD generator which was used for these studies, 0.291, and the asymmetry by the COMPHEP MC generator [34,35] used when calculating the theoretical predictions [4], 0.279. Part of the discrepancy can also be explained by the fact that the generated signal sample is an all inclusive  $e^+e^- \rightarrow b\bar{q}q\bar{q}q$  rather than  $e^+e^- \rightarrow t\bar{t} \rightarrow b\bar{b}q\bar{q}q\bar{q}$  as assumed in the theoretical paper. In any event, this difference is not significant for the purpose of sensitivity estimation.

## IX. CONCLUSION

We therefore conclude that the achievable resolution for the forward-backward asymmetry of the top quark

at the ILC in the  $e^+e^- \rightarrow t\bar{t} \rightarrow b\bar{b}q\bar{q}q\bar{q}$  channel is approximately 0.008 for a total luminosity of  $500 \text{ fb}^{-1}$ . Similarly, the achievable resolution for the  $b$  quark resulting from the top decay is also 0.008. In the case of polarized beams the achievable resolution for both the top and bottom quark asymmetries is 0.010 and 0.012 for the  $-80\%$  electron polarization,  $+30\%$  positron polarization and the  $+80\%$  electron polarization,  $-30\%$  positron polarization, respectively. This result allows us to constrain the theoretically predicted deviations from the standard model in the presence of an anomalous coupling of the  $Zt\bar{t}$  and  $Wtb$  vertices. In the case of the  $Zt\bar{t}$  coupling the resolution on the predicted standard model form factor is of the order of 0.05 and 0.04 for the  $F_{LZ}$  and the  $F_{RZ}$  couplings, respectively. In the case of the  $Wtb$  the performed analysis is sensitive to the presence of a  $B_L$  anomalous

form factor greater than approximately 0.05. The analysis employed realistic detector simulations and advanced reconstruction algorithms in the framework of the Silicon Detector concept. A new quark charge reconstruction algorithm used to discriminate between bottom quarks and their antiquarks allowed us to achieve a selection purity of up to 80% for an efficiency of about 60%.

## ACKNOWLEDGMENTS

We would like to thank the colleagues from the SiD software and benchmarking groups, in particular, Jan Strube, Tim Barklow, Norman Graf, and John Jaros for assistance with sample processing and useful discussions. The work of M. P. is supported by the U.S. Department of Energy under Contract No. DE-AC02-76SF00515.

- 
- [1] G. L. Kane, G. A. Ladinsky, and C. P. Yuan, *Phys. Rev. D* **45**, 124 (1992).
- [2] C. R. Schmidt, *Phys. Rev. D* **54**, 3250 (1996).
- [3] L. Brzezinski, B. Grzadkowski, and Z. Hioki, *Int. J. Mod. Phys. A* **14**, 1261 (1999); B. Grzadkowski and Z. Hioki, *Phys. Rev. D* **61**, 014013 (1999).
- [4] E. Boos, M. Dubinin, M. Sachwitz, and H. J. Schreiber, *Eur. Phys. J. C* **16**, 269 (2000).
- [5] A. Djouadi, Report No. ENSLAPP-A-365-92, pp. 108–111.
- [6] M. Jezabek, T. Nagano, and Y. Sumino, *Phys. Rev. D* **62**, 014034 (2000).
- [7] W. Bernreuther, O. Nachtmann, P. Overmann, and T. Schröder, *Nucl. Phys.* **B388**, 53 (1992).
- [8] R. S. Chivukula, S. B. Selipsky, and E. H. Simmons, *Phys. Rev. Lett.* **69**, 575 (1992); R. S. Chivukula, E. H. Simmons, and J. Terning, *Phys. Lett. B* **331**, 383 (1994).
- [9] K. Agashe, R. Contino, and R. Sundrum, *Phys. Rev. Lett.* **95**, 171804 (2005); R. Contino, T. Kramer, M. Son, and R. Sundrum, *J. High Energy Phys.* **05** (2007) 074.
- [10] C. F. Berger, M. Perelstein, and F. Petriello, in Proceedings of the 2005 Snowmass Workshop, edited by U. Nauenberg, <http://www.slac.stanford.edu/econf/C0508141/>.
- [11] SiD Collaboration, SiD Letter of Intent, arXiv:0911.0006v1, <http://silicondetector.org/display/SiD/LOI>.
- [12] J. Brau, Y. Okada, N. Walker *et al.*, arXiv:0712.1950.
- [13] H. Yamamoto, *J. Phys. Soc. Jpn.* **76**, 111014 (2007).
- [14] M. J. Charles, arXiv:0901.4670.
- [15] W. Kilian, T. Ohl, and J. Reuter, arXiv:0708.4233.
- [16] M. Moretti, T. Ohl, and J. Reuter, arXiv:hep-ph/0102195.
- [17] T. Sjostrand, S. Mrenna, and P. Skands, arXiv:hep-ph/0603175v2.
- [18] S. Agostinelli, J. Allison, K. Amako, J. Apostolakis, H. Araujo, P. Arce, M. Asai, D. Axen, S. Banerjee, G. Barrand *et al.*, *Nucl. Instrum. Methods Phys. Res., Sect. A* **506**, 250 (2003).
- [19] B. R. S. Catani, Y. L. Dokshitzer, M. Olsson, G. Turnock, and B. R. Webber, *Phys. Lett. B* **269**, 432 (1991).
- [20] D. Bailey *et al.*, *Nucl. Instrum. Methods Phys. Res., Sect. A* **610**, 573 (2009).
- [21] E. Devetak, D.Phil. thesis, <http://www.physics.ox.ac.uk/lcfi/LCFI/erikdevetakthesis.pdf>, 2009.
- [22] B. List and J. List, Report No. LC-TOOL-2009-001, [www-flc.desy.de/lcnotes/notes/](http://www-flc.desy.de/lcnotes/notes/).
- [23] R. Akers *et al.*, *Z. Phys. C* **66**, 19 (1995).
- [24] R. D. Field and R. P. Feynman, *Nucl. Phys.* **B136**, 1 (1978).
- [25] V. M. Abazov *et al.* (D0 Collaboration), *Phys. Rev. D* **74**, 112002 (2006).
- [26] J. Thom, Ph.D. thesis, Report No. SLAC-R-585, 2002.
- [27] A. Heister *et al.* (ALEPH Collaboration), *Eur. Phys. J. C* **38**, 147 (2004).
- [28] T. Aaltonen *et al.* (CDF Collaboration), *Phys. Rev. D* **83**, 112003 (2011).
- [29] V. M. Abazov *et al.* (D0 Collaboration), *Phys. Rev. Lett.* **98**, 041801 (2007).
- [30] V. M. Abazov *et al.* (D0 Collaboration), arXiv:1105.6287 [Phys. Rev. D (to be published)].
- [31] B. Grzadkowski, Z. Hioki, and M. Szafranski, *Phys. Rev. D* **58**, 035002 (1998).
- [32] C. R. Schmidt and T. L. Barklow, in *Proceedings of the 1995 APS DPF Meeting*, edited by S. Seidel (World Scientific, Singapore, 1995).
- [33] T. Aaltonen *et al.* (CDF Collaboration), *Phys. Lett. B* **674**, 160 (2009), and CDF Public Note 10333, 2011.
- [34] E. Boos *et al.*, *Nucl. Instrum. Methods Phys. Res., Sect. A* **534**, 250 (2004).
- [35] A. Pukhov *et al.*, arXiv:hep-ph/9908288.